analytical chemistry

pubs.acs.org/ac Article

Sensitive and Simultaneous Detection of SARS-CoV-2-Specific IgM/IgG Using Lateral Flow Immunoassay Based on Dual-Mode Quantum Dot Nanobeads

Chongwen Wang,* Xingsheng Yang, Bing Gu,* Haifeng Liu, Zihui Zhou, Luoluo Shi, Xiaodan Cheng, and Shengqi Wang*

Cite This: *Anal. Chem.* 2020, 92, 15542−15549 Read Online

ACCESS | Metrics & More | Article Recommendations | Supporting Information

ABSTRACT: A rapid and accurate method for detection of virus (SARS-CoV-2)-specific antibodies is important to contain the 2019 coronavirus disease (COVID-19) outbreak, which is still urgently needed. Here, we develop a colorimetric-fluorescent dual-mode lateral flow immunoassay (LFIA) biosensor for rapid, sensitive, and simultaneous detection of SARS-CoV-2-specific IgM and IgG in human serum using spike (S) protein-conjugated SiO_2@Au@QD nanobeads (NBs) as labels. The assay only needs 1 μL of the serum sample, can be completed within 15 min, and is 100 times more sensitive than the colloidal gold-based LFIA. Two detection modes of our biosensor are available: the colorimetric mode for rapid screening of the patients with suspected SARS-CoV-2 infection without any special instrument and the fluorescent mode for sensitive and quantitative analyses to determine the concentrations of specific IgM/IgG in human serum and detect the infection early and precisely. We validated the proposed method using 16 positive serum samples from patients with COVID-19 and 41 negative samples from patients with other viral respiratory infections. The results demonstrated that combined detection of virus-specific IgM and IgG via SiO_2@Au@QD LFIA can identify 100% of patients with SARS-CoV-2 infection with 100% specificity.

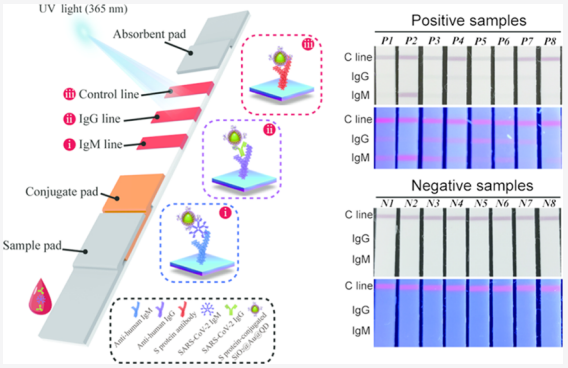

1. INTRODUCTION

In early December 2019, a newly emerging human infectious disease named coronavirus disease 2019 (COVID-19) was first reported in Wuhan city of China and confirmed to be caused by a severe acute respiratory syndrome coronavirus 2 (SARS-CoV-2).[1,2] COVID-19 has been declared as a pandemic on 12 March 2020 by the World Health Organization due to its rapid spread and high infective rate. Up to 15 August 2020, more than 21 026 000 confirmed cases have been reported worldwide, resulting in over 755 786 deaths (WHO COVID-19 Situation Report-208).[3] In the absence of specific drugs and vaccines for COVID-19, timely and accurate diagnosis is the only effective means to limit further spread of the virus and suppress the epidemic for saving lives. At present, nucleic acid-based detection methods, including real-time reverse transcription-polymerase chain reaction (RT-PCR) and sequencing, are the preferred tools for clinical diagnosis of SARS-CoV-2 infection.[4−6] Despite their good accuracy, RT-PCR and sequencing require long detection times (>2 h), special room to avoid contamination, expensive equipment, and trained operators, which hinder the application of these methods for point-of-care testing (POCT).

Serological test for specific antibodies of SARS-CoV-2 is a feasible approach for a simple and effective diagnosis of COVID-19.[7,8] Recent studies have shown that two kinds of virus-specific antibodies, namely, immunoglobulin-M (IgM) and immunoglobulin-G (IgG), generated by SARS-CoV-2 can be detected in patients' serum at early stages of the disease (<5 days).[9,10] Given that the concentrations of these antibodies significantly increase during the acute and convalescent phases of COVID-19, the detectable rates of IgM and IgG in patients increase to 94.1 and 100% within 19 days after symptom onset, respectively.[10] Moreover, the IgM level decreases rapidly in recovered patients by 3 weeks, whereas IgG titer is maintained at high levels even after 2 months.[7,12] Therefore, sensitive and simultaneous detection of virus-specific IgM and IgG can not only realize early and accurate identification of a SARS-CoV-2-infected person but also monitor the progress of the disease.

Colloidal gold (Au NP)-based lateral flow immunoassay (LFIA) is currently the most mature POCT method that has

Received: August 17, 2020
Accepted: November 9, 2020
Published: November 19, 2020

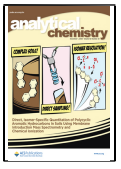

https://dx.doi.org/10.1021/acs.analchem.0c03484
Anal. Chem. 2020, 92, 15542−15549

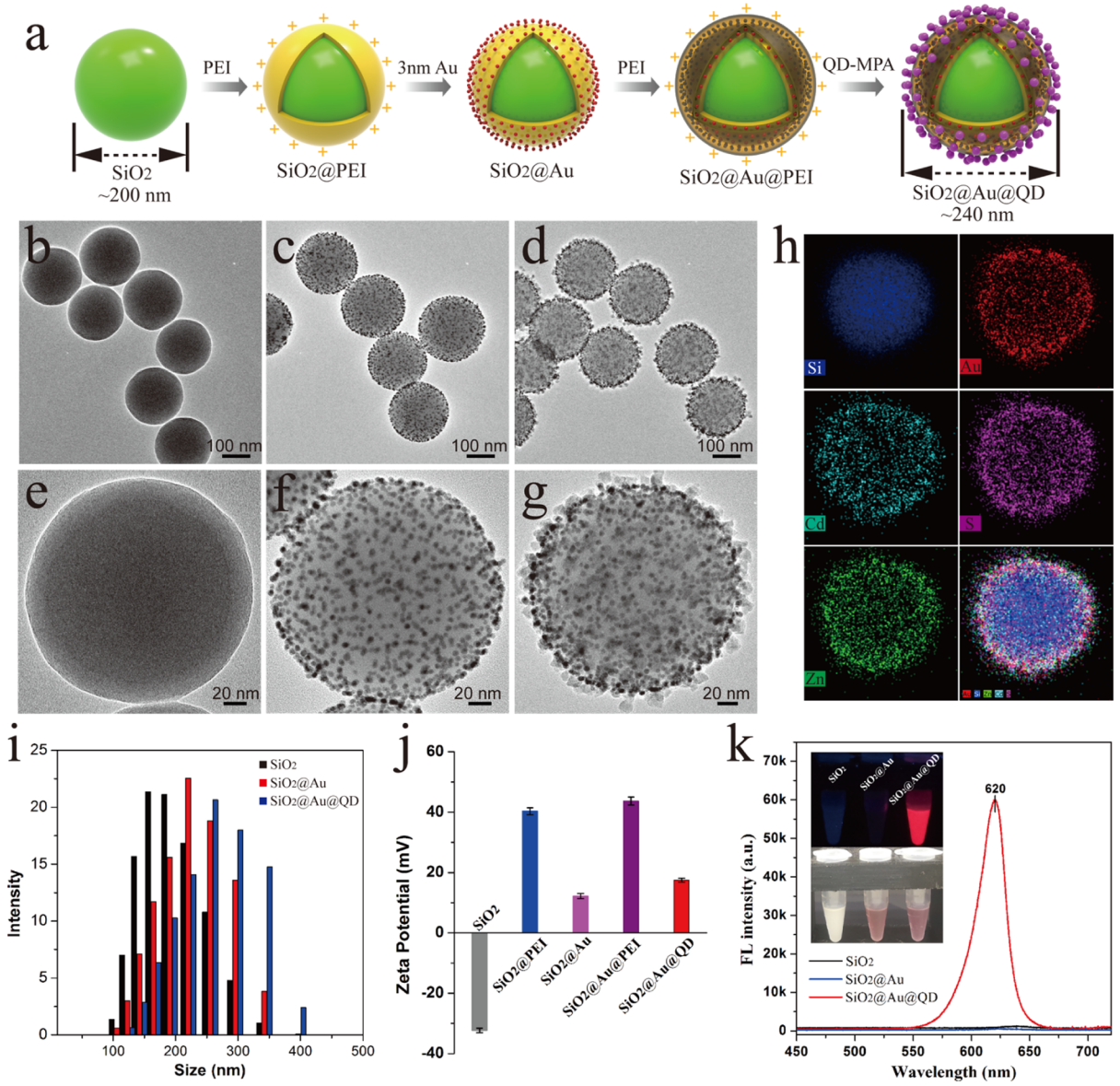

Figure 1. (a) Sequential process for fabricating dual-mode SiO_2@Au@QD fluorescent labels. TEM images of (b) SiO_2, (c) SiO_2@Au, and (d) SiO_2@Au@QD, with their corresponding magnified TEM images of a single particle in (e), (f), and (g), respectively. (h) Elemental mapping images of a single SiO_2@Au@QD NP. (i) DLS distribution of SiO_2 (black), SiO_2@Au (red), and SiO_2@Au@QD (blue). (j) ζ-Potentials of the products from each stage. (k) Fluorescence spectra of SiO_2, SiO_2@Au, and SiO_2@Au@QD under UV light. (Inset) Photographs of these particles under UV light (above) and visible light (below).

remarkable advantages of simple operation, rapid analysis, portability, and low cost.[13,14] The major drawback of the Au NP-based LFIA is the low sensitivity based on the colorimetric analysis; as such, this technique is not available for highly sensitive detection of targets. In recent years, quantum dots (QDs) are widely used as fluorescence labels in the LFIA system to improve sensitivity and quantitative ability because of their excellent optical properties, including quantifiable fluorescence intensity, broad excitation, and high light stability.[15−17] Nevertheless, a large-scale application of QD-based LFIA strip remains limited because common QDs are too small (5−20 nm) to centrifuge and are unstable for chemical modification. Additionally, a QD-based LFIA requires an additional UV light source or a commercial fluorescent reader for fluorescence signal measurement, which may be a burden for areas with poor medical conditions.

Our recently published works have proposed a polyethyleneimine (PEI)-mediated assembly method to fabricate Fe_3O_4@QD core−shell nanobeads (NBs) with excellent stability, high luminescence, and good biocompatibility using PEI-mediated electrostatic adsorption of numerous carboxylated QDs onto the Fe_3O_4 surface.[18−20] These Fe_3O_4@QD NBs are superior fluorescence labels of the LFIA system for complex sample detection. Based on these findings, herein, we designed and synthesized novel colorimetric-fluorescent dual-mode SiO_2@Au@QD NBs as a multifunctional label of the LFIA strip for simultaneous detection of SARV-CoV-2-specific IgM and IgG. The proposed SiO_2@Au@QD NBs consisted of three parts: a 200 nm monodisperse SiO_2 NP as the hydrophilic core, a layer of 4 nm Au NP-formed shell to generate a strong colorimetric signal, and a layer of carboxylated QD-formed shell to provide high luminescence

https://dx.doi.org/10.1021/acs.analchem.0c03484
Anal. Chem. 2020, 92, 15542−15549

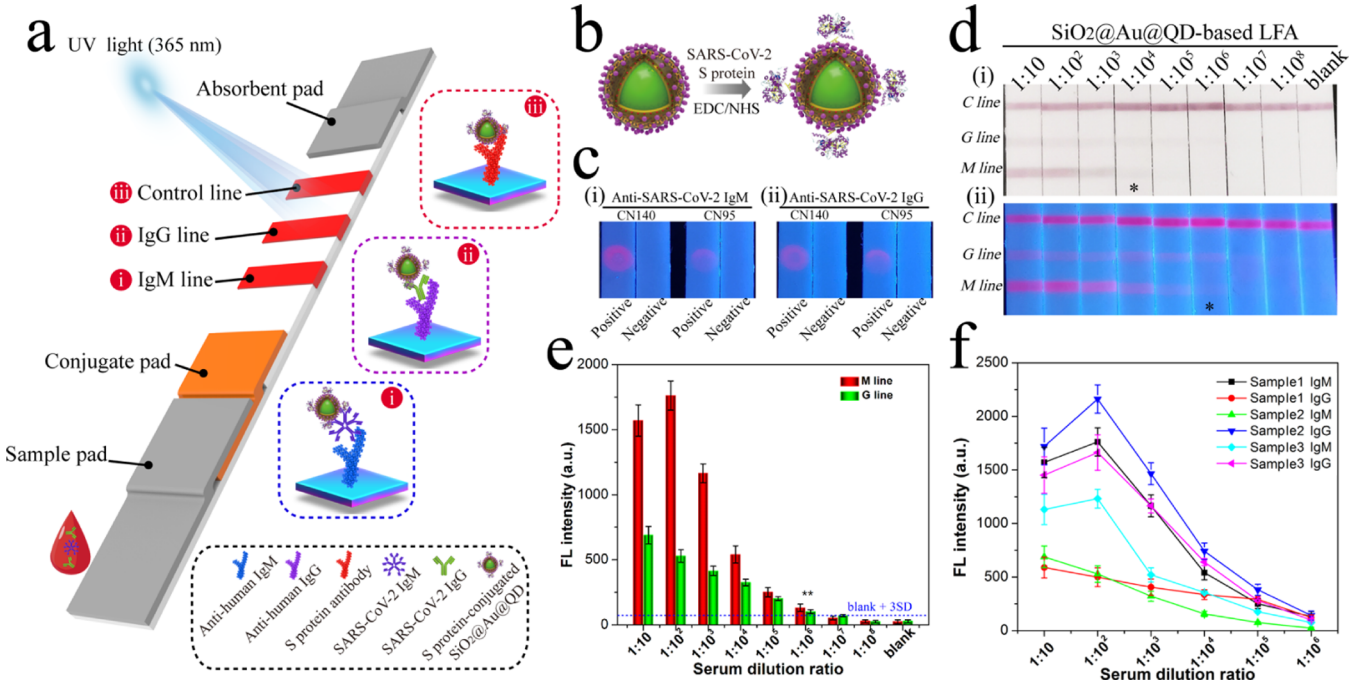

Figure 2. (a) Schematic of a dual-mode LFIA biosensor. (b) Preparation of S protein-conjugated SiO_2@Au@QD labels. (c) Optimization of NC membrane of LFIA. (d) Photographs and fluorescence images of the dual-mode LFIA for SARS-CoV-2-positive serum samples with different dilutions. (e) Corresponding fluorescence intensities of two test lines of the dual-mode LFIA. (f) Relationship of fluorescence intensity of test lines for three different positive serum samples with different dilutions.

and abundant surface sites for protein conjugation. The SARS-CoV-2 spike (S) protein was immobilized on the SiO_2@Au@QD surface, while antihuman IgM and IgG were modified on the two test lines of the strip to achieve sensitive detection of COVID-19. Sixteen clinical serum samples from patients with COVID-19 and 41 serum samples from patients with other viral respiratory infections were collected from the Affiliated Hospital of Xuzhou Medical University and tested with the proposed assay. The results demonstrated that our method has high sensitivity (100%) and specificity (100%) for detecting SARS-CoV-2 infection.

2. EXPERIMENTAL SECTION

2.1. Ethics Statement. All of the human serum samples, including 16 clinical serum samples from COVID-19 patients and 41 COVID-19-negative serum specimens, were provided by the Affiliated Hospital of Xuzhou Medical University. The 41 negative control sera were collected from the patients with other viral respiratory infections, including 31 cases of influenza A infection, 7 cases of influenza B infection, and 3 cases of respiratory syncytial virus infection. The study was conducted under the Declaration of Helsinki and approved by the Ethics Committee of the hospital with the case number of XYFY2020-KL016-01. All patients signed an informed consent.

2.2. Materials, Reagents, and Instrumentation. Bovine serum albumin (BSA), saccharose, and sodium azide (NaN_3) were provided by Sinopharm Chemical Reagent Co. Ltd. (Shanghai, China). Carboxyl-functionalized CdSe/ZnS QDs (Catalog #CdSe-MPA-625) were obtained from Mesolight Inc. (Suzhou, China). SARS-CoV-2 spike S1 protein (Catalog #40591-V08H) and SARS-CoV-2 spike antibody (Catalog #40150-R007) were purchased from Sino Biological Inc. (Beijing, China). Goat antihuman IgM, goat antihuman IgG, fetal bovine serum (FBS), branched PEI (MW ~25 kDa), poly(vinylpyrolidone) (PVP, MW 40 000), trisodium citrate (TSC), *N*-hydroxy-sulfosuccinimide (sulfo-NHS), tetraethoxysylane (TEOS), and *N*-(3-dimethylaminopropyl)-*N*′-ethylcarbodiimide hydrochloride (EDC) were obtained from Sigma-Aldrich (St. Louis). The nitrocellulose membrane (UniSart CN140 and CN95) was purchased from Sartorius (Göttingen, Germany). Other LFIA components, including the sample pads, absorbent pads, conjugate pads, and poly(vinyl chloride) (PVC) bottom plates, were provided by Jieyi Biotechnology Co (Shanghai, China).

Transmission electron microscopy (TEM) images of nanobeads (including SiO_2, SiO_2@Au, and SiO_2@Au@QD) were taken on a Tecnai G2 F20 microscope (Philips, Holland) at an accelerating voltage of 200 kV. ζ-potentials and dynamic light scattering (DLS) results were investigated using a Mastersizer 2000 (Malvern, U.K.). Fluorescence signal of SiO_2@Au@QD-based LFIA strip was acquired on a portable fluorescent instrument (365 nm excitation and 610 nm emission).

2.3. Preparation of 200 nm SiO_2 NPs. SiO_2 nanospheres (~200 nm) were prepared through a modified Stöber method.[21] In brief, 100 mL of ethanol was mixed with 6 mL of deionized water and 3.5 mL of ammonia solution (28%) under vigorous stirring. Then, 4 mL of TEOS was added into the above solution, and the mixture was stirred at room temperature for 5 h. The resulting SiO_2 NPs were purified twice by centrifugation and redispersed in 20 mL of ethanol.

2.4. Preparation of 4 and 40 nm Au NPs. The Au seed NPs (~4 nm) were synthesized via a sodium borohydride reduction method reported by Fang et al.[22] Briefly, 4 mL of 1% (w/w) TSC and 4 mL of 1% (w/w) $HAuCl_4$ solution were added into 392 mL of deionized water under vigorous stirring. Then, 6 mL of 0.2 M freshly prepared $NaBH_4$ was quickly

https://dx.doi.org/10.1021/acs.analchem.0c03484
Anal. Chem. 2020, 92, 15542−15549

added and the mixture was stirred continuously for 4 h. After that, 4 nm Au NPs were acquired and stored at 4 °C until use.

The Au NPs (~40 nm) were produced by a classical TSC reduction method.[23] Briefly, 2 mL of 1% (w/w) $HAuCl_4$ solution was mixed with 198 mL of deionized water, and the mixture was heated to boiling. After 2 min, 2.2 mL of 1% (w/w) TSC solution was rapidly added, and the solution was held at 100 °C with magnetic stirring for 15 min. Finally, the Au suspension was naturally cooled to room temperature and then stored at 4 °C.

2.5. Preparation of Dual-Mode SiO_2@Au@QD NBs. The colorimetric-fluorescent dual-mode SiO_2@Au@QD NBs were fabricated according to a PEI-mediated electrostatic adsorption strategy (Figure 1a). First, 0.5 mL of prepared SiO_2 NPs were incubated with a PEI solution (40 mL, 0.5 mg/mL) under sonication for 30 min. In the process, PEI was quickly coated on the SiO_2 surface as a positively charged layer. After washing twice to remove the nonreacting PEI, the resulting SiO_2@PEI NPs were redispersed in 10 mL of deionized water. Second, SiO_2@PEI NPs (10 mL) were mixed with abundant 4 nm Au NPs (100 mL) and sonicated for 30 min to form SiO_2@Au NPs. The obtained SiO_2@Au NPs were then collected by centrifugation (5500 rpm, 6 min) and dispersed in 5 mL of deionized water. Third, the prepared SiO_2@Au NPs were reacted with the PEI aqueous solution (50 mL, 0.5 mg/mL), and the mixture was sonicated for 60 min to coat the second PEI layer on the surface of SiO_2@Au NPs. After washing twice by centrifugation, SiO_2@Au@PEI was mixed with 20 mL of CdSe/ZnS-MPA QDs (1 nM) under sonication for 30 min to form a dual-mode SiO_2@Au@QD nanostructure. Finally, the synthesized SiO_2@Au@QD NBs were separated by centrifugation (5000 rpm, 6 min) and stored in 10 mL of ethanol.

2.6. Preparation of SARS-CoV-2 Spike Protein-Conjugated SiO_2@Au@QD. As illustrated in Figure 2b, a dual-mode SiO_2@Au@QD was functionalized with a SARS-CoV-2 S protein using carbodiimide chemistry. In brief, 1 mL of SiO_2@Au@QD was centrifuged, resuspended in 0.1 M 2-morpholinoethanesulfonic acid (MES) buffer (1 mL, pH 5.5), and then with 0.1 M EDC (10 μL) and 0.1 M sulfo-NHS (20 μL) under sonication for 15 min. The solution was centrifuged (4500 rpm, 6 min) to remove excess EDC/sulfo-NHS and resuspended in 10 mM phosphate-buffered saline (PBS) (200 μL, pH 7.4). Then, 10 μg of SARS-CoV-2 S protein was added into the mixture and then incubated for 2 h at room temperature under shaking at 800 rpm. The unreacted carboxyl groups on the SiO_2@Au@QD surface were blocked with 3% BSA for another 1 h. Finally, the S protein-conjugated SiO_2@Au@QD NBs were washed two times with PBS (10 mM, pH 7.4) by twice centrifugation (4500 rpm, 6 min) and resuspended in 300 μL of 10 mM PBS buffer containing 0.05% Tween-20 (v/v), 10% sucrose (w/v), 0.1% PVP (w/v), and 1% BSA (w/v). The S protein-conjugated labels were evenly dropped in the conjugate pad and freeze-dried in a vacuum.

2.7. Multiplex LFIA Strip Preparation for SARS-CoV-2-Specific IgM and IgG Simultaneous Detection. For SARS-CoV-2-specific IgM/IgG simultaneous detection, the LFIA strip was composed of four independent parts, including the sample pad, the conjugate pad, the NC membrane (CN140) with two test lines and a control line, and the absorption pad (Figure 2a). The two test lines (M line and G line) were separately sprayed onto antihuman IgM and IgG, whereas the control line (C line) was coated onto SARS-CoV-2 Spike antibody. Each antibody was sprayed onto the NC membrane with a dispense rate of 1 μL/cm via a spraying instrument and dried at 37 °C for 3 h. Finally, the LFIA strips were assembled and cut into 3 mm width for future use.

2.8. Analysis of Clinical Serum Samples via a Dual-Mode LFIA Strip. Human serum (1 μL) was added into 100 μL of running buffer, and the mixture was added onto the sample pad of an LFIA strip. As the liquid migrated from the sample pad toward the absorbent pad, S protein-conjugated labels were captured at the two test lines and control line, successively. After reaction for 15 min, the colorimetric signal and fluorescence signal on the two test lines were observed by naked eyes and recorded by a portable fluorescence reader (365 nm excitation), respectively. The LFIA detection was performed thrice for each serum sample, and the visible/fluorescence data were collected and analyzed.

3. RESULTS AND DISCUSSION

3.1. Fabrication and Characterization of SiO_2@Au@QD NBs. As illustrated in Figure 1a, dual-mode SiO_2@Au@QD NBs were fabricated based on a layer-by-layer assembly approach, which consisted of five consecutive steps as follows: (i) fabrication of 200 nm SiO_2 NPs as highly stable and monodispersed supporters, (ii) self-assembly of a layer of positively charged PEI on the SiO_2 surface, (iii) adsorption of dense negatively charged Au NPs (~4 nm) on the surface of SiO_2@PEI to produce a strong colorimetric signal, (iv) self-assembly of the second layer of PEI on the SiO_2@Au surface, and (v) adsorption of numerous carboxylated QDs on the second layer of PEI to provide a high fluorescence signal.

The fabricated SiO_2@Au@QD NBs were characterized by transmission electron microscopy (TEM), X-ray energy-dispersive spectroscopy (EDS), dynamic light scattering (DLS), and ζ-potential measurement. Figure 1b–d shows the TEM images of SiO_2, SiO_2@Au, and SiO_2@Au@QD NBs, respectively. With the successive formation of Au-NP shell and QD shell, the resulting SiO_2@Au and SiO_2@Au@QD remained monodispersed and their surface became rougher. When the dual-mode nanostructure was built, small Au NPs and QDs were added on the surface of the SiO_2 core layer upon layer. The magnified high-resolution TEM (HRTEM) images (Figure 1f,g) show the first layer of 4 nm Au NPs and the second layer of 12 nm CdSe/ZnS QDs on the surface of SiO_2. Figure 1h shows the EDS elemental mapping result of a single SiO_2@Au@QD NB. High concentrations of Si (blue) are concentrated on the core area; Au (red) is distributed on the Si surface; and Cd (azure), S (purple), and Zn (green) are observed on the outer layer of the nanostructure. These findings fully confirm the structural composition of SiO_2@Au@QD NBs. The DLS analysis shows that the hydrodynamic size of SiO_2@Au@QDs is ~240 nm, which is 28 and 40 nm larger than the sizes of SiO_2@Au and SiO_2 core, respectively (Figure 1i). All of these results indicate the successful preparation of SiO_2@Au@QD NBs. Meanwhile, the ζ-potentials of the nanocomposites increased greatly after PEI coating and decreased obviously after the adsorption of Au NPs and QDs (Figure 1j). The regular changes in the ζ-potential confirm that the LBL assembly of the SiO_2@Au@QD was driven by electrostatic adsorption.

The colorimetric and fluorescence properties of SiO_2@Au@QD NBs were assessed next. The UV–vis spectrum of SiO_2@Au@QD NBs was first investigated. In contrast to SiO_2 NPs,

https://dx.doi.org/10.1021/acs.analchem.0c03484
Anal. Chem. 2020, 92, 15542–15549

SiO_2@Au clearly displayed a strong absorption peak at 538 nm, which can be attributed to the plasmon resonance excitation from the 4 nm Au NP shell (Figure S1). After further adsorption of QDs, no obvious change in the UV−vis spectra was found for SiO_2@Au@QD NBs, suggesting that the QD shell did not affect the surface plasmon resonance of SiO_2@Au. Meanwhile, SiO_2@Au and SiO_2@Au@QDs exhibited purple-red color compared with SiO_2 NPs (inset of Figure 1k), suggesting their good colorimetric ability. After excitation with a 365 nm UV light, a bright-red fluorescence signal was observed for SiO_2@Au@QD NBs, whereas SiO_2 and SiO_2@Au showed no fluorescence emission (Figure 1k). The second layer of PEI ensured no direct contact between Au NPs and QDs. Our previous study has demonstrated that the thickness of the self-assembled PEI layer on the Ag shell was proportional to the reaction time and can reach 18 nm.[24] Herein, we found that the thickness of the PEI layer on the Au surface could be easily controlled in a range of 0−8 nm by adjusting the sonication time in the range of 0−60 min (Figure S2a−c). However, the maximum PEI thickness could not exceed 10 nm even when the sonication time increased to 120 min (Figure S2d−f). The ∼8 nm PEI layer corresponding to the sonication time of 60 min can effectively protect QDs against metal quenching (Figure S2g). The long-term stability of SiO_2@Au@QD NBs was investigated (Figure S3a), and their fluorescence intensity was stable within 60 days in ethanol. Moreover, SiO_2@Au@QD NBs were dispersed well in a high-salt solution (1 M), whereas common Au NPs generated serious aggregation in 10 mM NaCl solution (Figure S3b). The excellent optical/chemical stability of SiO_2@Au@QD NBs could be due to the use of highly stable SiO_2 cores and CdSe/ZnS QDs, and this property is critical to ensure the sensitivity and reliability of biosensors in complex samples.

3.2. Construction of a Dual-Mode LFIA for SARV-CoV-2-Specific IgM/IgG Detection. Figure 2a illustrates the dual-mode LFIA biosensor for simultaneous detection of anti-SARV-CoV-2 IgM and IgG in human serum using the SARS-CoV-2 S protein-conjugated SiO_2@Au@QD NBs. The components of the SiO_2@Au@QD-based LFIA include a sample pad, a conjugate pad for dual-mode label loading, an NC membrane with two test lines and one control zone, and an absorbent pad to provide capillary force. Antihuman IgM, antihuman IgG, and anti-S protein antibodies were dispensed on the test lines (M line and G line) and control line (C line), respectively. The clinical sample containing SARV-CoV-2-specific IgM and IgG antibodies was dropped onto the sample pad, which then migrated toward the absorbent pad by capillary force. During this process, the S protein-conjugated labels on the conjugate pad were quickly dissolved and bound to the target IgM/IgG by antibody−antigen reaction. The formed immunocomplexes continued to migrate along the NC membrane and were immobilized by human anti-IgM and anti-IgG antibodies on the two test zones. The excess SiO_2@Au@QD-S protein was captured by the anti-S protein antibody immobilized on the control zone. After chromatography, the two test lines showed visible/fluorescence bands in the presence of SARS-CoV-2-specific IgM and IgG, whereas only M line or G line exhibited visible/fluorescence band in the presence of one target IgM or IgG. A visible control line should be observed, which can indicate that the LFIA strip worked correctly. Notably, the fluorescence intensities of the IgM/IgG lines were proportional to the concentrations of the target antibodies in the clinical specimens, which could be easily read via a portable fluorescent instrument and used for SARS-CoV-2-specific IgM/IgG quantitative analysis.

Recent studies have shown that the S protein of SARS-CoV-2 has higher immunogenicity and specificity than other viral major structural proteins (including nucleocapsid protein) for serodiagnosis of COVID-19.[9,11] Thus, we chose S protein to modify labels to ensure the specificity and sensitivity of the biosensor. As demonstrated in Figure 2b, the S protein was directly conjugated to the COOH groups of SiO_2@Au@QDs through EDC/NHS-based covalent coupling. The ζ-potential of SiO_2@Au@QDs decreased with increasing antigen amount (5−15 μg) and remained stable at −17.1 mV, indicating the saturated loading of the S protein (Figure S4). Several key assay conditions of the LFIA biosensor were optimized. The types of the NC membrane were assessed first because they strongly affected the transport of the dual-mode label on the strip. As shown in Figure 2c, CN140 (8 μm pore size) and CN95 (15 μm pore size) membranes provided good transport of SiO_2@Au@QD NBs, whereas CN140 membrane generated higher fluorescence signals for IgM and IgG detection. The effect of the concentration of the antibodies loaded on the test lines was next evaluated. As shown in Figure S5a,b, 0.9 mg/mL of antihuman IgM and 1.2 mg/mL of antihuman IgG were respectively loaded on the corresponding test lines to achieve the highest signal-to-noise ratio (SNR) of the fluorescence intensity. The effect of reaction time on the test lines was also investigated, and the results showed that 15 min of test time is suitable for LFIA detection (Figure S5c).

Under optimal conditions, the detection performance of the dual-mode LFIA biosensor was evaluated by testing SARS-CoV-2-positive serum samples from patients with COVID-19. We performed this process by detecting a serially diluted positive serum specimen (from 1:10 to $1:10^8$ dilution). Figure 2d(i),(ii) displays the photographs and fluorescence images of test LFIA with two separate test lines for SARV-CoV-2-specific IgM/IgG detection. The purple color bands on M line and G line were observed with the naked eye, and these bands were derived from the colorimetric signal of the immobilized SiO_2@Au@QDs [Figure 2d(i)]. The purple bands on the test lines were visible at $1:10^4$ dilution of the positive serum samples. The result shows that the colorimetric detection ability of the SiO_2@Au@QD LFIA is equivalent to the traditional Au NP-based LFIA (Figure S6). In addition, the fluorescence intensities of the two test lines decreased with increasing dilution multiple of serum specimens (10× to 10^6×). The fluorescence signal on the test lines was observed at a dilution level of $1:10^6$. Thus, the overall sensitivity of the dual-mode LFIA based on SiO_2@Au@QD NBs was 100 times more than that of the commonly used Au-based LFIA strips for the detection of SARV-CoV-2-specific IgM/IgG. In addition, the detection ability of the dual-mode LFIA was compared with the SiO_2@QD-based fluorescent LFIA for the same positive sera, and the result was revealed in Figure S7. It shows that SiO_2@Au@QD LFIA can provide equivalent fluorescence sensitivity as the SiO_2@QD-based LFIA strip but has a unique colorimetric-fluorescent dual-mode detection ability. Only a high-dose "hook" effect with decreased visual fluorescence intensity for M line was observed in the 1:10 dilution level. The corresponding fluorescence signal of Figure 2d(ii) is recorded in Figure 2e, and the detection limit of the positive serum (from patient 1) was determined to be $1:10^6$ dilution by fluorescence values. The limit was calculated as the concentration corresponding to 3 times the standard deviation

https://dx.doi.org/10.1021/acs.analchem.0c03484
Anal. Chem. 2020, 92, 15542−15549

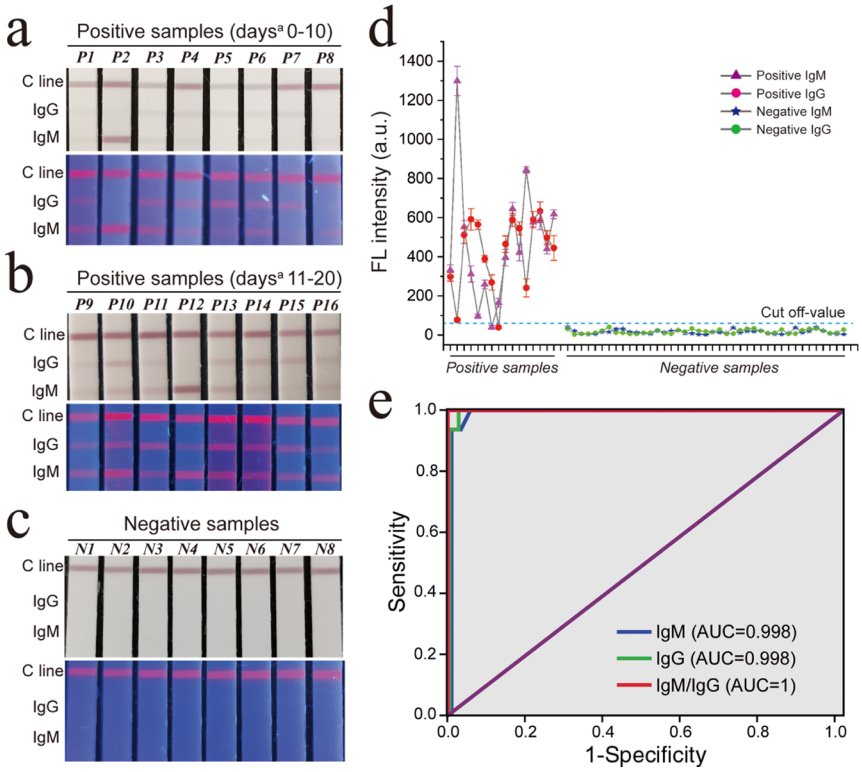

Figure 3. Photographs and fluorescence images of dual-mode LFIA applied in 16 positive serum specimens of patients with COVID-19 at different stages after disease onset (a, b), and 8 of 41 negative serum specimens (c). (d) Fluorescence intensities on the two test lines of the corresponding LFIA. The error bars indicate the standard deviations calculated from three separate tests. (e) ROC analysis to assess the detection capability of the proposed assay[a]a Days post-disease onset..

of the blank control measurement. Considering the influence of the hook effect on the detection accuracy, three positive serum specimens from patients with COVID-19 at different stages were diluted and then tested using the biosensor. As shown in Figure 2f, the $1{:}10^2$ dilution effectively reduced the hook effect on the strong positive serum and generated sufficient high-intensity signal for weak positive serum detection. Thus, we chose $1{:}10^2$ dilution of the serum samples for testing. All of these results indicate the advantages of the dual-mode LFIA for serodiagnosis of COVID-19. The colorimetric signal can be used for field testing to obtain rapid and high-throughput screening of strong positive samples, while the fluorescence signal can be employed for highly sensitive and quantitative detection of weak positive serum samples.

To ensure the activity and stability of SiO_2@Au@QD LFIA, the prepared LFIA strips were sealed in an aluminum foil bag containing a desiccant gel and stored at room temperature before use. As shown in Figure S8, the colorimetric signal and fluorescence intensity of the test lines were stable after 90 days of storage.

3.3. Evaluation of the Dual-Mode LFIA. To further evaluate the clinical feasibility of our proposed dual-mode LFIA, we tested 16 positive serum specimens (P1−P16) collected from patients with COVID-19 who were diagnosed by RT-PCR and 41 negative serum specimens from patients with other viral respiratory infections (N1−N41). According to the stages after disease onset, the 16 positive serum specimens were divided into two groups: early-stage group (P1−P8: collected between 0 and 10 days after symptom onset) and late-stage group (P9−P16: collected between 11 and 20 days after symptom onset). As presented in Figure 3a, the visual results from the colorimetric signal were difficult to be discerned by the naked eye, and only the M line of P2−P3 and the G line of P3−P7 were clearly observed. In fluorescence detection mode, most of the test lines exhibited obvious fluorescence band, except that no clear G line of two samples (P2 and P8) and the M line of P7 were distinguished. Direct comparison of the colorimetric and fluorescence signals demonstrated that the latter resulted in a brighter and clearer signal with a higher sensitivity. Figure 3b shows that the colorimetric signal on the test lines became more distinct, and only the G line of P12 was difficult to identify. Meanwhile, all the test lines exhibited a clear fluorescence band. The overall fluorescence intensities (G line + M line) of most of the samples in the late-stage group were stronger than those in the early-stage group. This phenomenon can be explained by the fact that the concentrations of specific IgM and IgG increase as the disease progresses. Figures 3c and S9 show a bright control line for all the 41 negative samples, and no other colorimetric/fluorescence signals were observed on the strip by the naked eye. This finding indicates good accuracy and specificity of the proposed method. The corresponding fluorescent values of all 16 positive serum specimens and 41 negative samples were recorded (Figure 3d). The cutoff values of SiO_2@Au@QD LFIA for IgM and IgG via fluorescence signal were calculated as 42 and 40 a.u., respectively, which was defined as the average signal intensities of the negative samples plus 3 times the standard deviation. Moreover, the ROC curve was used to validate the diagnostic power of our method. As shown in Figure 3e, the ROC curves revealed the integrated area under the curve (AUC) values of 0.998, 0.998, and 1 for SARS-CoV-

https://dx.doi.org/10.1021/acs.analchem.0c03484
Anal. Chem. 2020, 92, 15542−15549

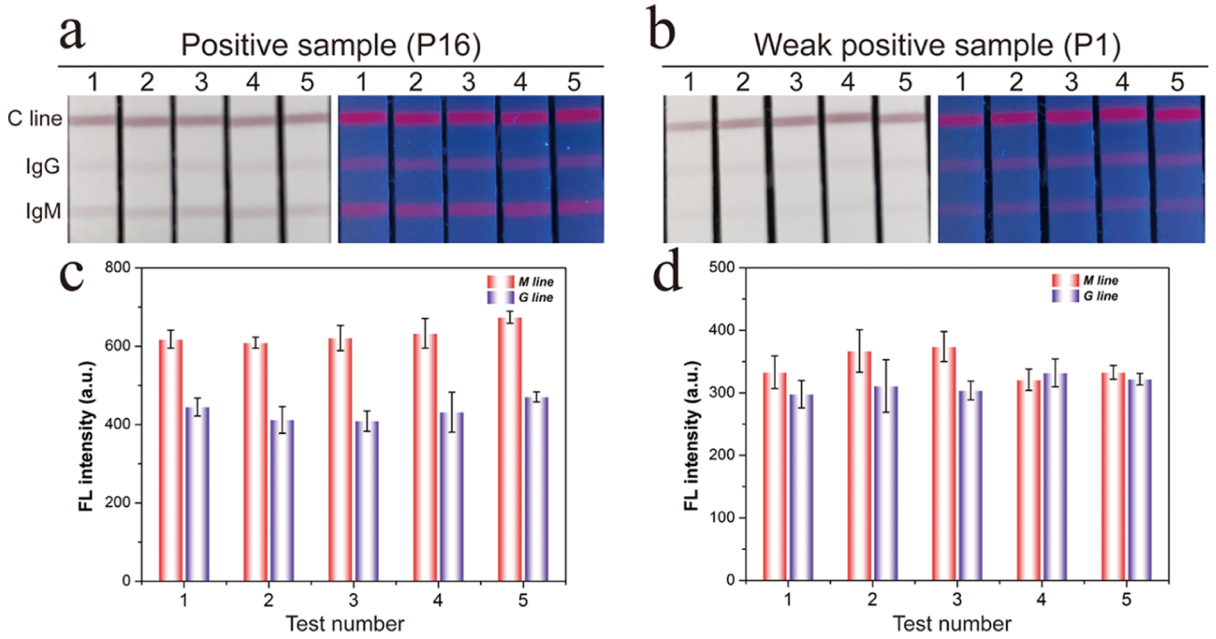

Figure 4. Assay reproducibility of the dual-mode LFIA. Photographs and fluorescence images of five independent tests for (a) a moderate positive serum specimen (P16) and (b) a weak positive serum specimen (P1). Corresponding fluorescence intensities of two test lines for P16 serum (c) and P1 serum (d).

2-specific IgM, IgG, and IgM/IgG combined detection, indicating the excellent accuracy of the proposed biosensor. In addition, the dual-mode LFIA had good repeatability for SARS-CoV-2-specific IgM and IgG simultaneous detection with low relative standard deviation (ranging from 3.5 to 6.7%) (Figure 4). Recent studies revealed that SARS-CoV-2-specific IgG titer was maintained at high levels for a long period in infected persons, whereas the IgM levels decreased markedly 1 month after the disease onset.[11,25] The SiO_2@Au@QD LFIA-based IgM−IgG combined assay exhibits the potential to detect trace amounts of virus-specific IgM/IgG in early samples and to help assess the disease course by analyzing the concentrations of IgM and IgG in positive serum.

4. CONCLUSIONS

This study describes a new class of dual-mode LFIA biosensor for rapid and sensitive detection of SARS-CoV-2-specific IgM/IgG in clinical samples. By taking advantages of SiO_2@Au@QD labels in the LFIA system, we were able to sensitively and simultaneously detect low concentrations of IgM/IgG ($1{:}10^6$ dilution) from 1 μL of serum within 15 min. The performance and cutoff values of our biosensor were determined using 57 clinical samples (16 positive serum samples and 41 negative samples). The IgM/IgG combined detection sensitivity was determined to be 100% and its specificity can reach 100%, indicating the great potential of our proposed method for rapid and accurate screening of SARS-CoV-2-infected persons in the field.

■ ASSOCIATED CONTENT

Supporting Information

The Supporting Information is available free of charge at https://pubs.acs.org/doi/10.1021/acs.analchem.0c03484.

Additional experimental description (S1: preparation of Au NP-based LFIA strip; S2: preparation of S protein-conjugated SiO_2@QD NBs), clinical sample information of the COVID-19 patients (Table S1), and supporting figures (Figures S1−S9) mentioned in the main text (PDF)

■ AUTHOR INFORMATION

Corresponding Authors

Chongwen Wang − *College of Life Sciences, Anhui Agricultural University, Hefei 230036, P. R. China; Beijing Institute of Radiation Medicine, Beijing, P. R. China;* orcid.org/0000-0002-9627-107X; Email: wangchongwen1987@126.com

Bing Gu − *Medical Technology Institute of Xuzhou Medical University, Xuzhou 221004, P. R. China; Department of Laboratory Medicine, Affiliated Hospital of Xuzhou Medical University, Xuzhou 221004, P. R. China;* Email: gb20031129@163.com

Shengqi Wang − *Beijing Institute of Radiation Medicine, Beijing, P. R. China;* orcid.org/0000-0003-0380-5659; Email: sqwang@bmi.ac.cn

Authors

Xingsheng Yang − *College of Life Sciences, Anhui Agricultural University, Hefei 230036, P. R. China; Beijing Institute of Radiation Medicine, Beijing, P. R. China*

Haifeng Liu − *College of Life Sciences, Anhui Agricultural University, Hefei 230036, P. R. China; Beijing Institute of Radiation Medicine, Beijing, P. R. China*

Zihui Zhou − *College of Life Sciences, Anhui Agricultural University, Hefei 230036, P. R. China; Beijing Institute of Radiation Medicine, Beijing, P. R. China*

Luoluo Shi − *Medical Technology Institute of Xuzhou Medical University, Xuzhou 221004, P. R. China*

Xiaodan Cheng − *College of Life Sciences, Anhui Agricultural University, Hefei 230036, P. R. China; Beijing Institute of Radiation Medicine, Beijing, P. R. China*

Complete contact information is available at:

https://dx.doi.org/10.1021/acs.analchem.0c03484
Anal. Chem. 2020, 92, 15542−15549

https://pubs.acs.org/10.1021/acs.analchem.0c03484

Notes

The authors declare no competing financial interest.

■ ACKNOWLEDGMENTS

This study was supported by the National Natural Science Foundation of China (Grant Nos. 81830101, 81471994, and 81871734) and the Natural Science Foundation of Anhui Province (Grant No. 1908085QB85). We thank Beijing Zhongkebaice Technology Service Co., for helping to conduct TEM and DLS analysis.

■ REFERENCES

(1) Li, Q.; Guan, X.; Wu, P.; Wang, X.; Zhou, L.; Tong, Y.; Ren, R.; Leung, K. S. M.; Lau, E. H. Y.; Wong, J. Y.; Xing, X.; Xiang, N.; Wu, Y.; Li, C.; Chen, Q.; Li, D.; Liu, T.; Zhao, J.; Liu, M.; Tu, W.; Chen, C.; Jin, L.; Yang, R.; Wang, Q.; Zhou, S.; Wang, R.; Liu, H.; Luo, Y.; Liu, Y.; Shao, G.; Li, H.; Tao, Z.; Yang, Y.; Deng, Z.; Liu, B.; Ma, Z.; Zhang, Y.; Shi, G.; Lam, T. T. Y.; Wu, J. T.; Gao, G. F.; Cowling, B. J.; Yang, B.; Leung, G. M.; Feng, Z. *N. Engl. J. Med.* **2020**, *382*, 1199−1207.

(2) Coronaviridae Study Group of the International Committee on Taxonomy of Viruses. The species Severe acute respiratory syndrome-related coronavirus: classifying 2019-nCoV and naming it SARS-CoV-2*Nat. Microbiol.*20205536544 DOI: 10.1038/s41564-020-0695-z.

(3) WHO. Coronavirus Disease 2019 (COVID-19): Situation Report-208. https://www.who.int/docs/default-source/coronaviruse/situation-reports/20200815-covid-19-sitrep-208.pdf?sfvrsn=9dc4e959_2 (accessed August 15, 2020).

(4) Wölfel, R.; Corman, V. M.; Guggemos, W.; Seilmaier, M.; Zange, S.; Müller, M. A.; Niemeyer, D.; Jones, T. C.; Vollmar, P.; Rothe, C.; Hoelscher, M.; Bleicker, T.; Brünink, S.; Schneider, J.; Ehmann, R.; Zwirglmaier, K.; Drosten, C.; Wendtner, C. *Nature* **2020**, *581*, 465−469.

(5) Cui, F.; Zhou, H. S. *Biosens. Bioelectron.* **2020**, *165*, No. 112349.

(6) Broughton, J. P.; Deng, X.; Yu, G.; Fasching, C. L.; Servellita, V.; Singh, J.; Miao, X.; Streithorst, J. A.; Granados, A.; Sotomayor-Gonzalez, A.; Zorn, K.; Gopez, A.; Hsu, E.; Gu, W.; Miller, S.; Pan, C. Y.; Guevara, H.; Wadford, D. A.; Chen, J. S.; Chiu, C. Y. *Nat Biotechnol.* **2020**, *38*, 870−874.

(7) Xu, X.; Sun, J.; Nie, S.; Li, H.; Kong, Y.; Liang, M.; Hou, J.; Huang, X.; Li, D.; Ma, T.; Peng, J.; Gao, S.; Shao, Y.; Zhu, H.; Lau, J. Y.; Wang, G.; Xie, C.; Jiang, L.; Huang, A.; Yang, Z.; Zhang, K.; Hou, F. F. *Nat. Med.* **2020**, *26*, 1193−1195.

(8) Zhao, J.; Yuan, Q.; Wang, H.; Liu, W.; Liao, X.; Su, Y.; Wang, X.; Yuan, J.; Li, T.; Li, J.; Qian, S.; Hong, C.; Wang, F.; Liu, Y.; Wang, Z.; He, Q.; Li, Z.; He, B.; Zhang, T.; Fu, Y.; Ge, S.; Liu, L.; Zhang, J.; Xia, N.; Zhang, Z. *Clin. Infect. Dis.* **2020**, No. ciaa344.

(9) Liu, W.; Liu, L.; Kou, G.; Zheng, Y.; Ding, Y.; Ni, W.; Wang, Q.; Tan, L.; Wu, W.; Tang, S.; Xiong, Z.; Zheng, S. *J. Clin. Microbiol.* **2020**, *58*, No. e00461-20.

(10) Xiang, F.; Wang, X.; He, X.; Peng, Z.; Yang, B.; Zhang, J.; Zhou, Q.; Ye, H.; Ma, Y.; Li, H.; Wei, X.; Cai, P.; Ma, W. L. *Clin. Infect. Dis.* **2020**, *71*, 1930−1934.

(11) Long, Q. X.; Liu, B. Z.; Deng, H. J.; Wu, G. C.; Deng, K.; Chen, Y. K.; Liao, P.; Qiu, J. F.; Lin, Y.; Cai, X. F.; Wang, D. Q.; Hu, Y.; Ren, J. H.; Tang, N.; Xu, Y. Y.; Yu, L. H.; Mo, Z.; Gong, F.; Zhang, X. L.; Tian, W. G.; Hu, L.; Zhang, X. X.; Xiang, J. L.; Du, H. X.; Liu, H. W.; Lang, C. H.; Luo, X. H.; Wu, S. B.; Cui, X. P.; Zhou, Z.; Zhu, M. M.; Wang, J.; Xue, C. J.; Li, X. F.; Wang, L.; Li, Z. J.; Wang, K.; Niu, C. C.; Yang, Q. J.; Tang, X. J.; Zhang, Y.; Liu, X. M.; Li, J. J.; Zhang, D. C.; Zhang, F.; Liu, P.; Yuan, J.; Li, Q.; Hu, J. L.; Chen, J.; Huang, A. L. *Nat. Med.* **2020**, *26*, 845−848.

(12) Hou, H.; Wang, T.; Zhang, B.; Luo, Y.; Mao, L.; Wang, F.; Wu, S.; Sun, Z. *Clin. Transl. Immunol.* **2020**, *9*, No. e01136.

(13) Nguyen, V. T.; Song, S.; Park, S.; Joo, C. *Biosens. Bioelectron.* **2020**, *152*, No. 112015.

(14) Chen, Z.; Zhang, Z.; Zhai, X.; Li, Y.; Lin, L.; Zhao, H.; Bian, L.; Li, P.; Yu, L.; Wu, Y.; Lin, G. *Anal. Chem.* **2020**, *92*, 7226−7231.

(15) Hu, J.; Zhang, Z. L.; Wen, C. Y.; Tang, M.; Wu, L. L.; Liu, C.; Zhu, L.; Pang, D. W. *Anal. Chem.* **2016**, *88*, 6577−6584.

(16) Qie, Z.; Liu, Q.; Yan, W.; Gao, Z.; Meng, W.; Xiao, R.; Wang, S. *Anal. Chem.* **2019**, *91*, 9530−9537.

(17) You, P. Y.; Li, F. C.; Liu, M. H.; Chan, Y. H. *ACS Appl. Mater. Interfaces* **2019**, *11*, 9841−9849.

(18) Wang, C.; Xiao, R.; Wang, S.; Yang, X.; Bai, Z.; Li, X.; Rong, Z.; Shen, B.; Wang, S. *Biosens. Bioelectron.* **2019**, *146*, No. 111754.

(19) Wang, C.; Shen, W.; Rong, Z.; Liu, X.; Gu, B.; Xiao, R.; Wang, S. *Nanoscale* **2020**, *12*, 795−807.

(20) Rong, Z.; Bai, Z.; Li, J.; Tang, H.; Shen, T.; Wang, Q.; Wang, C.; Xiao, R.; Wang, S. *Biosens. Bioelectron.* **2019**, *145*, No. 111719.

(21) Asadirad, A. M.; Branda, N. R. *J. Am. Chem. Soc.* **2015**, *137*, 2824−2827.

(22) Fang, Y.; Guo, S.; Zhu, C.; Zhai, Y.; Wang, E. *Langmuir* **2010**, *26*, 11277−11282.

(23) Li, J. F.; Tian, X. D.; Li, S. B.; Anema, J. R.; Yang, Z. L.; Ding, Y.; Wu, Y. F.; Zeng, Y. M.; Chen, Q. Z.; Ren, B.; Wang, Z. L.; Tian, Z. Q. *Nat. Protoc.* **2013**, *8*, 52−65.

(24) Wang, C.; Li, P.; Wang, J.; Rong, Z.; Pang, Y.; Xu, J.; Dong, P.; Xiao, R.; Wang, S. *Nanoscale* **2015**, *7*, 18694−18707.

(25) Li, Z.; Yi, Y.; Luo, X.; Xiong, N.; Liu, Y.; Li, S.; Sun, R.; Wang, Y.; Hu, B.; Chen, W.; Zhang, Y.; Wang, J.; Huang, B.; Lin, Y.; Yang, J.; Cai, W.; Wang, X.; Cheng, J.; Chen, Z.; Sun, K.; Pan, W.; Zhan, Z.; Chen, L.; Ye, F. *J. Med. Virol.* **2020**, *92*, 1518−1524.